Materialia 7 (2019) 100394

Contents lists available at ScienceDirect

Materialia

journal homepage: www.elsevier.com/locate/mtla

Full Length Article

Graphite interface mediated grain-boundary sliding leads to enhanced mechanical properties of nanocrystalline silicon carbide

Kolan Madhav Reddy[a,1,*], Dezhou Guo[b,1], Simanta Lahkar[a], Chun Cheng[c], Yutaka Shinoda[d], Qi An[b,*], Xiaodong Wang[a,*]

[a] State Key Laboratory of Metal Matrix Composites, School of Materials Science and Engineering, Shanghai Jiao Tong University, Shanghai 200240, PR China
[b] Chemical and Materials Engineering Department, University of Nevada, Reno, NV 89557, USA
[c] WPI Advanced Institute for Materials Research, Tohoku University, Sendai 980-8577, Japan
[d] Materials and Structures Laboratory, Tokyo Institute of Technology, 4259-R3-24, Nagatsuta, Midori, Yokohama, Japan

ARTICLE INFO

Keywords:
Silicon carbide
Interfaces
Mechanical properties
Transmission electron microscopy
Molecular dynamics

ABSTRACT

Mechanical properties and microstructural deformation characterization of nanocrystalline silicon carbide (n-SiC) have been studied at room-temperature by using nanoindentation and uniaxial microcompression tests abetted with Raman spectroscopy and transmission electron microscopy (TEM). The enhanced mechanical properties of n-SiC observed from indentation and uniaxial micropillars compression tests is mainly attributed to nano-size effect and soft interface phase at the grain boundaries. TEM reveals that the n-SiC upon deformation undergoes grain boundary sliding with the assistance of graphitic interface phase thereby enhancing the strength, fracture toughness and plasticity. The critical crack length values estimated for n-SiC are two to three orders of magnitude smaller than that usually found for brittle ceramics, which implies that plasticity can be achieved before crack initiation and failure. Our density functional theory molecular dynamics simulations agree with the experimental results and provide an atomistic insight in which the graphite along the grain boundary facilitates the grain boundaries sliding in n-SiC.

1. Introduction

Among high performance ceramics, cubic silicon carbide (β-SiC) exhibiting a low specific density offers outstanding properties such as high hardness and stiffness, good thermal and electrical conductivity, excellent creep and wear resistance, which are promising for electronic and structural applications [1,2]. However, the major limitation of currently employed β-SiC ceramics were prone to catastrophic failure because of rigid covalent bonding [3–5]. In addition, secondary phases and porosity greatly influence strength and toughness when the final component is subject to mechanical loading [5–7].

Usually, β-SiC is fabricated by pressureless sintering above 2000 °C temperature with an addition of sintering aids such as carbon and boron or aluminium [1,8,9]. These sintering aids are primarily used to remove the surface layers contamination of SiC particles and to enhance thermal diffusivity during the densification [8,9]. Thus, the obtained sintering microstructure possesses strong interfacial bonding between the micro-size SiC grains, leading to a poor fracture toughness of about 2 to 3 MPa $m^{1/2}$, and fractures transgranularly [10–12]. Several attempts have been made to enhance the fracture toughness by modifying the conventional SiC microstructure through a liquid phase sintering (LPS) at relatively low temperatures in the range of 1800 °C to 1950 °C [13–17]. The enhanced fracture toughness of LPS-SiC was mainly attributed to plate-like grains formed during the in-situ phase transition from cubic to hexagonal SiC crystal structure [15–18]. Although the accomplished microstructure through LPS process produces a high fracture toughness between 5 and 8 MPa $m^{1/2}$ by the intergranular fracture mode [16–18], it was found in practical applications that stress concentration builds up around the elongated grains during mechanical deformation, leading to the reduction of strength and creep properties [1,10,19].

According to the well-known Hall–Petch relationship, grain refinement is considered as a promising way to enhance the mechanical properties of solid materials without changing their chemical composition [20]. In recent years, there have been significant experimental efforts to synthesize nanostructured SiC [21,22]. For example, Vassen and Stöver reported the dense sintered microstructure with a mean grain size of below 100 nm using hot isostatic pressing technique [23]. The measured hardness ranged from 23 to 26 GPa and the fracture toughness was between 2.5 to 3.5 MPa $m^{1/2}$ [23]. Later Shindo et al. found large ductility up to 140% for the fine grained SiC in compressive tests at high

* Corresponding authors.
E-mail addresses: kmreddy@sjtu.edu.cn (K. Madhav Reddy), qia@unr.edu (Q. An), xdwang77@sjtu.edu.cn (X. Wang).
[1] These authors contributed equally to this work.

https://doi.org/10.1016/j.mtla.2019.100394
Received 27 May 2019; Accepted 29 June 2019
Available online 02 July 2019

temperatures of 1600–1800 °C [24]. More recently Liao et al. synthesized nanocrystalline β-SiC thin films with less than 20 nm grain sizes and achieved a high hardness between 30 and 50 GPa [25]. Even though these studies showed the increase in hardness and toughness of β-SiC due to its nano-size effect compared to their conventional coarse grain counterparts, the underlying deformation mechanism responsible for the enhanced mechanical properties has not been verified experimentally.

In particular, enhanced mechanical properties of nanocrystalline ceramics may give rise to unique plastic deformation mechanisms that are not found in coarse-grained polycrystals [26,27]. For instance, Szlufaraka et al. performed molecular dynamics (MD) simulations on nanosized SiC with 80–85% crystallinity and found the crossover plasticity from intergranular to intragranular dominated deformation occurs by a combination of cooperative grain sliding, grain rotations, and intergranular dislocation formation [28]. Although MD simulations indicate an essential role of switching from the dominated by crystalline to deformation dominated by disordering, the understanding of localized underlying deformation process between SiC and interface phase have not been forthcoming.

In this work, we report the mechanical properties of nanocrystalline SiC (n-SiC) with a uniform graphitic phase at the grain boundaries (GBs). We found that the nano-layered graphitic interface phase in n-SiC is effective in enhancing toughness, strength and plasticity. TEM and density functional theory molecular dynamics (DFT-MD) revealed that the grain boundary sliding mechanism is responsible for the extraordinary properties of n-SiC with the assistance of graphite phase at high contact pressures.

2. Experimental procedure

2.1. Sample preparation

Ultrafine β-SiC powder was prepared by the gas-phase reaction of $SiCl_4$, SiH_4, CH_4, and C_2H_4 (T-1 grade, Sumitomo-Osaka Cement Co., Tokyo, Japan). The ultrafine SiC powders measured using transmission electron microscopy ranges from 20 to 70 nm in size (Supplementary Fig. S1). The powder contained 3.5 wt% of free carbon and 0.41 wt% of oxygen, and the amount of metallic impurities was <1 ppm. The starting β-SiC contained free carbon, which were trapped at the surfaces of the fine powders. The β-SiC powders were die pressed at a pressure of 40 MPa with dimensions of 15 mm*5 mm specimens. The compacts were first coated with BN powder to avoid reaction with glass tubes. Then they were densified by cold isostatic pressing (CIPing) under 200 MPa in vacuum encapsulated within pyrex^{TM}-type glass tube (Iwaki glass co., Chiba, Japan) at a temperature of about 760 °C [24]. Finally, the capsules were held at a temperature of 800 °C in an argon atmosphere for 1.2×10^3 s in a special HIP equipment and isostatically pressed at 1600 °C and 980 MPa for 3.6×10^3 s.

The obtained sintered specimens were polished with successive grades of diamond lapping films to reduce the contribution of surface roughness on the measurements of mechanical properties. The final density of the sintered SiC compact was determined by the Archimedes' method with deionized water as the immersion medium.

2.2. Mechanical properties measurements

A dynamic ultra-micro-hardness tester (shimadzu W201S) equipped with a Berkovich indenter was used to carry out hardness and fracture toughness measurements at maximum loads ranging from 200 to 1000 mN at a constant loading rate (7.06 mN/s).

The micropillars with an aspect ratio of 3:1 (height: diameter) were prepared by a focused ion beam (FIB) system (JEOL JIB-4600F). A large diameter pool was made to guarantee that the flat punch is in contact only with the pillars during compression test. These micropillars were loaded in uniaxial compression at a constant loading rate of 0.33 mN/s using a nanodevice (Shimadzu W201S) and tests were performed using flat punch indenters with diameters of 10 μm and 40 μm.

2.3. Characterization

XRD measurements were carried out on bulk polished sintered specimens in a Rigaku X-ray diffractometer (RINT 2200) with an X-ray Cu tube (CuK_α, λ= 1.5418 Å). XRD patterns were collected over a 2θ range from 20° to 70° with a step width of 0.5° and $2\theta^o$/min. Phase identification was done using the JCPDS database. Crystallite size (D) was determined using the Scherer formula. $D = \frac{0.9\ \lambda}{\beta\cos\theta}$, where λ is the wavelength of x-rays, θ is the diffraction angle, and β is the corrected half width. Fracture toughness was evaluated from scanning electron microscope (JEOL, JIB-4600F) images by measuring the diagonal and crack lengths of residual impression made by indentation. Raman spectra were acquired to monitor the pressure-induced structural transition using a Renishaw micro-Raman spectrometer equipped with a charge coupled device (CCD) detector and a microscope for focusing the incident laser beam to a ~1 μm spot size. A 514.5 nm Ar ion laser was used as the excitation source. The spectrum was collected at a lower laser power in order to avoid local heating effects. TEM was performed using a JEOL JEM-ARM 200F operated at 200 kV equipped with spherical aberration (Cs) correctors of both probe-forming and image-forming lenses. As synthesized TEM specimen were sliced from the bulk n-SiC sintered compact and were mechanically ground to a thickness of 100 μm. The surface of the specimen was then dimpled to a thickness of about 20 μm and ion-beam milled to obtain electron transparency by using a low angle ion milling (Fischione 1010). The cross-sectional TEM specimens of both the pristine surface and the deformed n-SiC were prepared by the lift-out technique using an FIB system (FEI Versa3D) for detailed microstructure characterization. Prior to TEM, the cross sectioned specimens were gently cleaned using Nano mill at 500 eV for 15 min to remove the induced damage layers caused by FIB system without altering the surface chemistry. The high-resolution images were acquired using scanning TEM mode (STEM). Average grain size values and interface thickness were calculated from the STEM images using the Image Tool software.

2.4. Computational simulations

To illustrate how the graphite interface determines the deformation mechanism of n-SiC, we employed density functional theory (DFT) based molecular dynamics (DFT-MD) simulations to examine the mechanical response of a laminated SiC-graphite structure under a finite shear deformation. The laminate structure was constructed by combining the SiC and graphite supercells. We focused on the shear deformation along $(111)\langle\bar{2}11\rangle$ slip system of SiC, which is expected to be favorable for the formation of dislocations as suggested by the experimental observations. We chose (001) slip plane of graphite. The lattice mismatch is minimized by replicating SiC 4 times along x and y directions, and graphite 5 times along x and y direction, respectively. To minimize the Van der Waals interaction between SiC with graphite layers, the graphite layer is shifted to maximum the atomic distance between SiC and graphite layers. The model contains 392 atoms in total, including 96 Si and 296 C atoms, respectively. For the sake of computational convenience, we rotated the supercell, in which the x–y plane is the (111) slip plane and x-axis is along the $\langle\bar{2}11\rangle$ slip direction for SiC, and the x–y plane is the (001) slip plane and x-axis is along the $\langle100\rangle$ slip direction for graphite in a Cartesian coordinate system.

The laminated structure is optimized using DFT implemented in VASP package with a plane-wave basis set [29,30]. The Perdew–Burke–Ernzerh (PBE) functional and the projector augmented-wave (PAW) method are applied for the exchange-correlation interaction and the core-valence interaction, respectively [31,32]. The pseudo potentials in PAW method consider the $2s^22p^2$ electrons and $3s^23p^2$ electrons as valence states for C and Si elements, respectively. The tetrahedron method with Blöchl corrections was applied to determine the electron partial

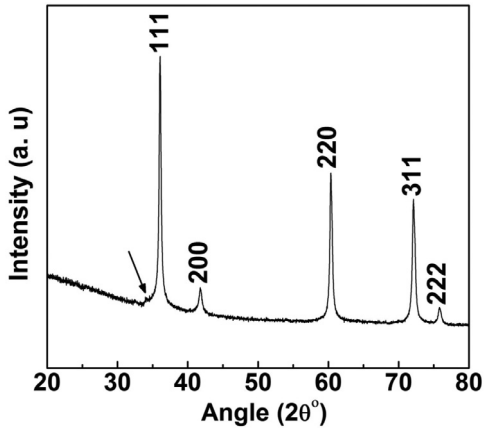

Fig. 1. XRD pattern of n-SiC sintered at temperature and pressure of 1600 °C and 980 MPa. The arrow mark indicates the planar faults in the microstructure. All the crystalline intensity peaks are assigned to SiC cubic phase.

occupancies [33]. The kinetic energy cutoff was set to 500 eV for the plane wave expansions. The convergence criteria were set to 1×10^{-5} eV and 1×10^{-2} eV Å^{-1} for the electronic self-consistent field (SCF) procedure and ionic relaxation loop, respectively. The Brillouin zone integration was performed on Γ-centered symmetry-reduced Monkhorst–Pack meshes with $1\times1\times1$ k-point grid mesh. We considered the van der Waals interactions using DFT-D3 method with Becke–Jonson damping approach [34]. Periodic boundary conditions are applied along all three directions. The optimized cell parameters at 0 K are $a=12.36$ Å, $b=12.36$ Å, $c=28.26$ Å, $\alpha=\beta=90^{\circ}$, and $\gamma=120^{\circ}$.

The model was pre-deformed with various uniaxial pre-compressed ratios perpendicular to the slip plane to mimic the compressed conditions in our indentation experiments. On the basis of the deformation and stress conditions in indenter region, we consider 10% and 15% uniaxial compression perpendicular to the slip plane which is comparable to our experiments. Each compressed model was first optimized at 0 K, and then heated to 300 K for 5 ps using the NVT ensemble (constant volume, constant temperature, and constant number of atoms) with the Nose–Hoover thermostat to obtain the equilibrium structure at ambient conditions, and finally sheared at a constant shear rate of 0.02/ps.

3. Results

3.1. As synthesized silicon carbide characterization

Nanocrystalline silicon carbide (n-SiC) powders containing 3.5 wt% excessive free carbon were sintered at a relatively low temperature to obtain the fine grained microstructure using high pressure hot isostatic pressing. The measured final densities of bulk sintered nanocrystalline silicon carbide (n-SiC) are 97% (3.12 g/cc) by considering excessive carbon content. X-ray diffraction (XRD) spectra shows all crystalline peaks correspond to the β-SiC phase, while the low concentration carbon not detected in spectra might be due to insensitivity of XRD detector (Fig. 1). The crystallite size estimated from XRD using the Scherer's method for the planes of (111), (220), and (311) were 23.1 nm, 22 nm, and 19.5 nm reveals that the as-sintered bulk SiC with symmetric grains. A shoulder peak observed on the left tail of (111) peak at about 2θ=33.6° attributed to presence of planar defects in SiC microstructure [22,35].

Low magnification TEM image shows as-sintered SiC is almost fully dense, consisting of nearly equiaxial nanograins (Fig. 2a). A selected area electron diffraction (SAED) taken from the region of Fig. 2a confirms that these β-SiC with randomly distributed grains (Inset Fig. 2a). Fig. 2b zoom in TEM image displays that these n-SiC grains are encapsulated with carbon phase. A representative high resolution TEM (HRTEM) image taken from grain boundary interface reveal the graphitic carbon

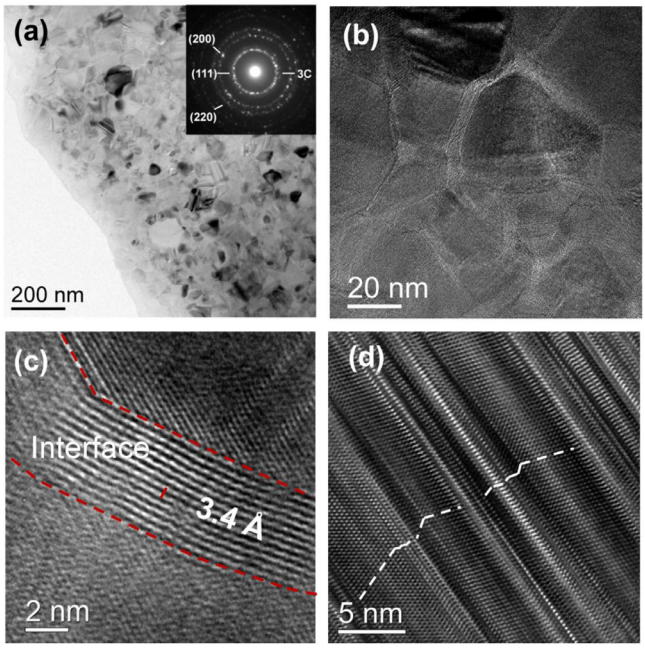

Fig. 2. (a) TEM image of as-sintered n-SiC shows fine grained microstructure. The SAED pattern confirms only single phase cubic SiC (Inset). (b) Magnified TEM image display uniformly encapasculated carbon surrounded by SiC nanograins. (c) A representative high resolution TEM image shows crystalline carbon with graphitic lattice at the grain boundary interface. (d) High density of nanotwins and stack faults within n-SiC grain.

with a lattice spacing distance of about ~0.34 nm (Fig. 2c). HRTEM of Fig. 2d shows a high density of nanotwins and stacking faults, but no other defects such as dislocations were found in as-sintered n-SiC.

The bright field (BF) and dark field (DF) STEM images show evidence of equiaxial SiC nano-grains with the uniform distribution of graphitic carbon phase at the grain boundaries as well as at triple junctions as shown in Fig. 3a and b, as well as Supplementary Fig. S2. The statistical measurement of STEM images revealed grain sizes in the range of ~10 to 100 nm with a mean and standard deviation of 35±15 nm (Fig. 3c). The estimated widths of the graphitic carbon grain boundaries were in between ~0.68 nm and 8 nm (Fig. 3d). These microstructural examinations suggest that the as-sintered n-SiC growth is controlled by the presence of nano-layered carbon phase at the grain interface and use of relatively low temperature sintering restricts the grain growth to nanometer grains.

3.2. Hardness and elastic modulus measurements

Fig. 4 shows Load–depth (p–h) curves obtained with the Bervoich indenter for various loads ranging from 200 mN to 1000 mN at the constant loading rate of 7.06 mN/s. The curves appear smooth and regular without any large bursts during loading-unloading cycles [36]. By determining the contact area, A, and the contact stiffness (S),$= {}^{dP}/_{dh}$, from the maximum applied load, $P_{\max}$, and the peak displacement, $h_{\max}$, from the p–h curves, hardness (H) of n-SiC was evaluated according to the nano-indentation equation [37]:

$$H = {}^{P_{max}}/_{A_c} \tag{1}$$

where, H-hardness, P_{max}-peak load, A_c-contact area

The elastic modulus of n-SiC is determined from 20% of unloading curve using the below equation [38]

$$\frac{1}{E_r} = \frac{1-\upsilon^2_m}{E_m} + \frac{1-\upsilon^2_i}{E_i} \tag{2}$$

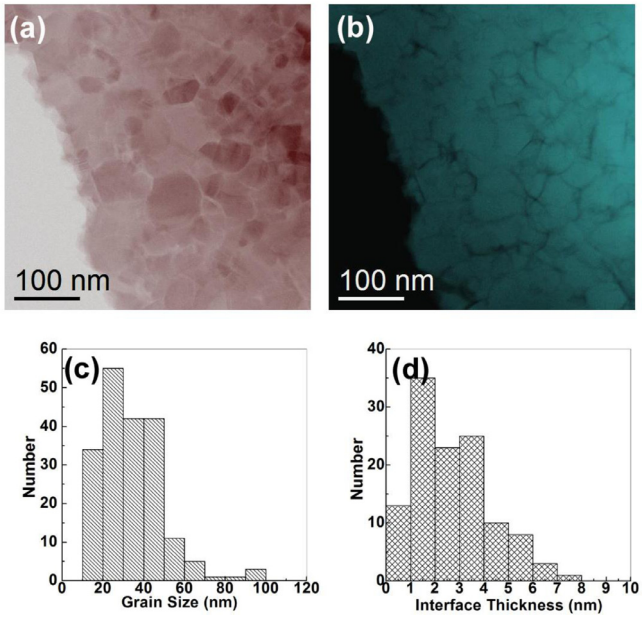

Fig. 3. (a) BF-STEM, and (b) DF-STEM images of as-sintered β-SiC showing nanograined microstructure with uniformly distributed carbon at the grain boundary interface phases. (c) The SiC grain size ranging from ~10–100 nm with a mean 35±12 nm. (d) carbon interface thickness ranges from ~0.7 nm to 8 nm.

where the constant β is 1.034 for the berkovich indenter, ν_i and E_i possion's ratio and elastic modulus of diamond tip, while E_m and ν_m are elastic modulus and possion's ratio of the current material, respectively.

The calculated H and E values of n-SiC as a function of the applied loads are shown in Fig. 4. The obtained H and E ranges from 35 to 23 GPa and 470 to 310 GPa, respectively. The observed indentation size effect may be associated with strain gradient plasticity [39]. The H and E values of n-SiC were improved compared to that of microcrystalline H and E values, which ranges in between 18 and 23 GPa and 330–360 GPa, but less than the reported nanocrystalline SiC films values, which are between 30–50 GPa and 265–515 GPa [1,10,23,25]. The low H and E of n-SiC as compare to nanocrystalline SiC films mainly attributed to the presence of weak graphite interface phase.

3.3. Fracture toughness measurements

The fracture toughness (K_{IC}) was calculated from the lengths of radial cracks emanating from corners of the berkovich indents using following equation [38,40].

$$K_{Ic} = x_V \left(\frac{a}{l}\right)^{1/2} \left(\frac{E}{H}\right)^{2/3} \frac{P}{C^{3/2}} \quad (3)$$

P is the applied load; E is the elastic Modulus; H is the indentation hardness

x_V –constant (0.016); c is radial crack length (measured from the center of indent); a is half of the square diagonal.

The measured (K_{IC}) value of n-SiC ranges from 3.3 to 5.4 MPa $m^{1/2}$ from low to high loads (Fig. 5a and Supplementary Fig. S3). Fig. 5b illustrates well-developed radial crack morphology from n-SiC indent edges applied at 1000 mN, and within the residual indent region no cracks appeared.

3.4. Raman spectroscopy analysis

The representative Raman spectra from pristine surface and indented region of n-SiC under the excitations of 514.5 nm laser are shown in Fig. 6. Inset SEM image shows the residual indentation at load of 1000 mN. In the low frequency region below 1000 cm^{-1}, the spectra of pristine n-SiC show two bands at 796 cm^{-1} and 968 cm^{-1} corresponding to transverse (TO) and longitudinal (LO) modes of strain free cubic SiC (in curve A) [41]. In the high frequency region above 1000 cm^{-1}, the spectra display the graphitic carbon peaks, located at 1360 cm^{-1}, 1590 cm^{-1}, 1620 cm^{-1}, 2450 cm^{-1} and 2700 cm^{-1}. The 1360 cm^{-1} and 1620 cm^{-1} peaks are attributed to defect-induced D band, ~1590 cm^{-1} peak is assigned to in-plane vibrational G band, 2450 cm^{-1} peak is the non-dispersive band and 2700 cm^{-1} peak is the two-phonon 2D (G^1) band [42,43]. Fig. 6 (curve B) readily shows changes in the Raman peak intensity and broadening can be observed upon indentation. Consequently, the measured Raman bands intensity of I(D)/I(G) increases to 1.65 and 2(D)/I(G) increases to 1.15 upon indentation showing an increase in the degree of disorder in the graphitic phase. On the other hand, only broadening for SiC peaks was noticed which indicates no crystal-to-crystal structural transition upon deformation (Fig. 6).

3.5. Microstructural characterization of deformed nanocrystalline sic

In order to determine the underlying deformation mechanism responsible for enhanced mechanical properties of n-SiC, a cross sectional TEM specimen was prepared from the residual indent using focused ion beam (FIB) milling. A typical TEM specimen preparation is shown in Fig. 7 for the indented region at the maximum load of 1000 mN. The indent cross sectioned specimen of n-SiC was sliced using FIB milling and then thinned down to less than 50 nm foil for TEM observations [44,45]. Fig. 8a and b shows that the BF-STEM and DF-STEM images were simultaneously recorded. The bright and dark contrast features at grain boundaries in the images of Fig. 8a and b display diffusive interface within the deformed n-SiC region, in contradiction to sharp interfaces

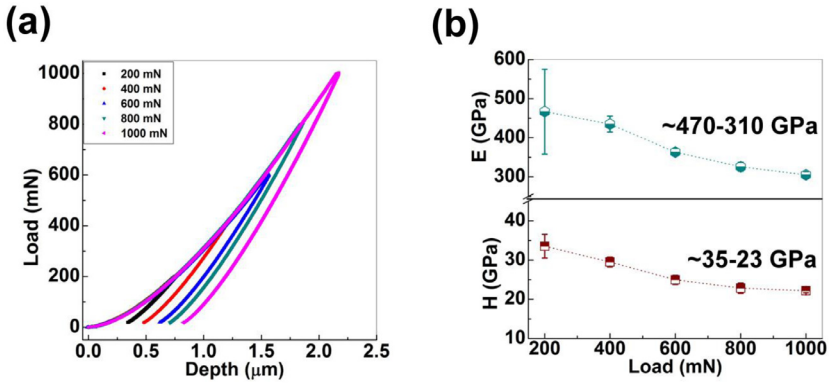

Fig. 4. Typical load-depth curves obtained from Bervoich nanoindenter on smoothly polished n-SiC surface under loads ranging from 200mN to 1000 mN at constant loading rate of 7.06 mN/s. (b)The hardness and elastic modulus is plotted against applied loads.

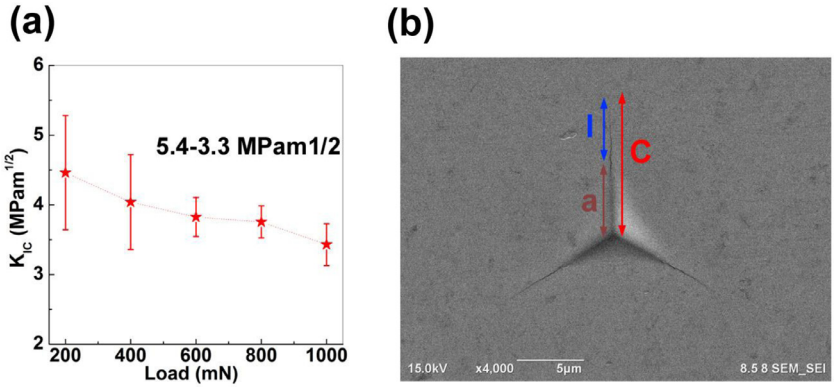

Fig. 5. (a) Fracture toughness mean values ranges from 5.4 to 3.3 MPam$^{1/2}$ from low to high loads. (b) A representative SEM image of a Berkovich indenter impression showing the determination of the geometric parameters used in Eq. (6) for the calculation of fracture toughness: a is the contact radius; c is the crack length; and l is the crack length emanating from the indent corner.

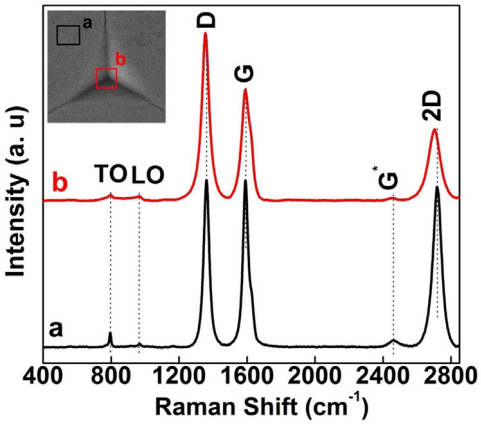

Fig. 6. Raman spectra shown for as-sintered surface (black curve) and residual indent region (red curve). The TO and LO corresponds to SiC and D, G, G* and 2D to graphitic carbon.

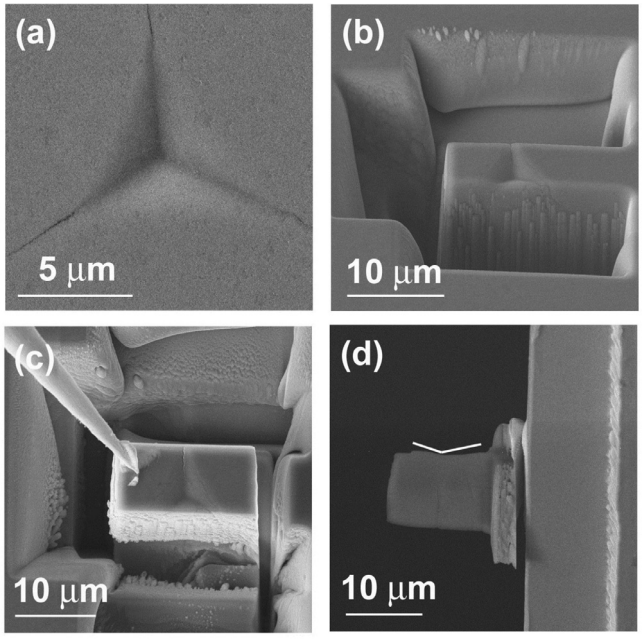

Fig. 7. The cross sectional TEM specimen prepared using focused ion beam milling. (a) SEM image shows the residual indent impression produced at maximum load of 1000 mN. (b) Large trenches made around the residual indents. (c) Specimen is attached with omni-probe by assistance of tungsten deposit. (d) Thin foil of n-SiC was attached to cu grid.

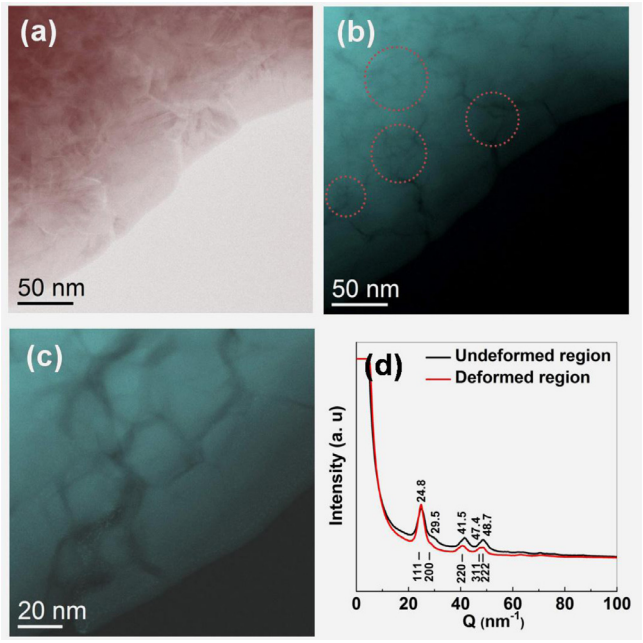

Fig. 8. (a) A representative bright field and (b) dark field STEM images taken from a residual indent region of n-SiC. The dark field STEM image showing a clusters of nano-grained size (<20 nm) within the deformed region. (c) Zoom-in DF-STEM image reveals no cracks appearance in fine grains sliding region (d) Electron diffraction intensity profile analysis shown before and after deformation.

of undeformed region (Fig. 3a and b). In addition, Fig. 8a and b show many fine grain clusters, which are typical <20 nm and are marked in red dotted circles. These fine grained SiC entities in the cluster form (see Fig. 8b) were free of interface carbon phases indicating that the small pores ~3% in as-sintered allows the motion of grain sliding within the deformation region. A zoom-in DF-STEM image (Fig. 8c) demonstrates that the smaller SiC grains experience shear sliding that is triggered by high stresses within the indent region. Moreover, no cracks appeared within the residual indent region indicating primarily intrinsic toughening [5,46]. The electron diffraction intensity curves (Fig. 8d) of undeformed and deformed regions show only cubic SiC phase. The obtained scattering vector (Q) peak positions are analogous to the XRD Bragg's angle (θ) determined by using equation $Q = 4\pi \sin(\theta)/\lambda$, showing undetectable crystal-to-crystal phase transition upon deformation.

Fig. 9 BF-STEM image taken from residual indent of n-SiC shows the evidence for the transition of grain boundary carbon interface. Fig. 9a image displays that the graphitic carbon transforms to highly disordered carbon at grain boundaries and triple junctions suggesting that

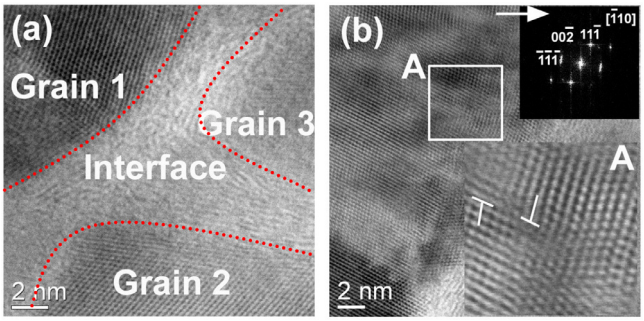

Fig. 9. A plane view bright field STEM image obtained within deformed n-SiC. (a) Image shows highly disordered carbon at grain boundary interface of SiC nanograins marked with red dotted lines. (b) Image display the visible dislocations on the {111} plane for the [110] direction of n-SiC.

nano grains may have experienced tremendous shear deformation by grain boundary sliding as the accommodation mechanism. A representative BF-STEM image taken at the proximity of grain interface along the $<\bar{1}10>$ direction within the deformed region is shown in Fig. 9b. Inset fast Fourier transform (FFT) pattern of Fig. 9b indicates that dislocations in the SiC grain have the Burger vector of $1/2<\bar{1}10>$ on the {111} primary slip plane. Further zoom-in inset image of Fig. 9b reveals emission of dislocations along the $(11\bar{1})$ glide plane of SiC, which suggests high local shear stresses produced on the smaller SiC grains during shear sliding deformation. Moreover, dislocations produced near the grain boundary interface also confirm load transfer and mobility of grains entity during the grain boundary (GB) sliding process. Furthermore, dislocation induced plasticity in n-SiC likely plays an additional role in redistributing internal stresses in order to accommodate grains sliding during shear deformation. Therefore, enhanced mechanical properties of n-SiC are attributed to the substantial sliding of small SiC grains with the assistance of carbon interface at high stresses by which accommodates the local plastic deformation to delay crack initiation and failure.

3.6. Uniaxial strength measurements

The deformation behavior of n-SiC was further investigated by uniaxial micro-compression testing. The diameters of the pillar specimens were shown in a range of 1 μm to 13.5 μm and with an aspect ratio of about 3: 1 (Fig. 10). The micropillars were fabricated using FIB milling and the template SEM image for the diameter of 3.15 μm is shown in Fig. 10a. The representative engineering stress–strain curves of micropillars with diameters of 2.75 μm, 3.15 μm and 13.5 μm, respectively, are shown in Fig. 10b. The fracture strength as a function of micro-pillar diameter size is plotted in Fig. 10c. It can be seen that for all the pillars the strength was above 8 GPa and the maximum strength is as high as ~11 GPa which is significantly higher than that of microcrystalline SiC (2–4 GPa) [47,48]. The SEM image of deformed micropillar revealed intergranular dominated fracture process for the n-SiC (Fig. 10d). More interestingly, n-SiC pillars exhibit non-elastic deformation before the failure as shown in inset Fig. 10b.

To understand the underlying mechanism responsible for the ultrahigh strength and detectable plasticity of n-SiC under uniaxial deformation, fractured surface of n-SiC was gently collected onto TEM cu-grid. BF-TEM image of the fractured n-SiC morphology shows high strain in carbon interface (Fig. 11a) as compare to the former undeformed region (Fig. 2b and d) indicating change in structures at or near grain boundaries of SiC nanograins. The high resolution BF-STEM image oriented along [101] zone axis shows edge dislocations near boundary of n-SiC grains (Fig. 11b). The emissions of dislocations along the {111} plane in nanograins suggests the applied high stresses during deformation may have reached the resolved shear stress and yield plastically before the crack initiation occurs.

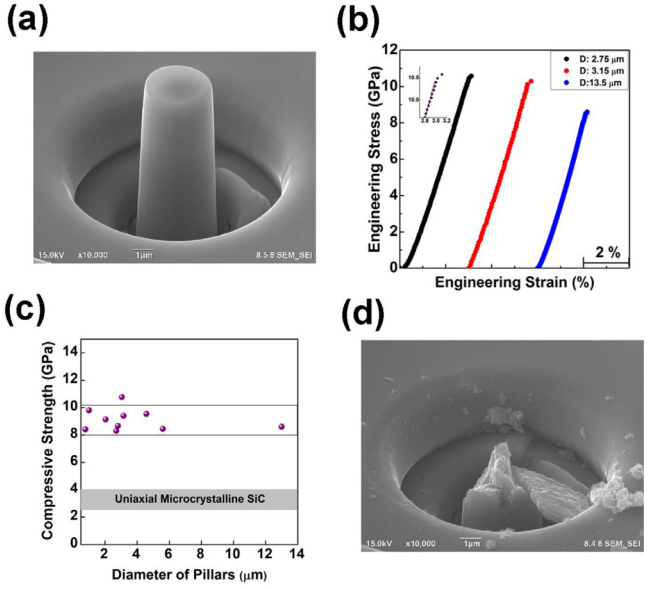

Fig. 10. (a) Engineering stress vs. engineering strain plot shown for different n-SiC compressed micropillars at constant loading 0.33 mN/s. Note the detectable plasticity before micropillars fracture. (b) Strength of n-SiC obtained on compression of different pillars diameter. (c) Typical fabricated micropillar using FIB milling. (d) Fractured micropillar reveals typical intergranular fracture mode.

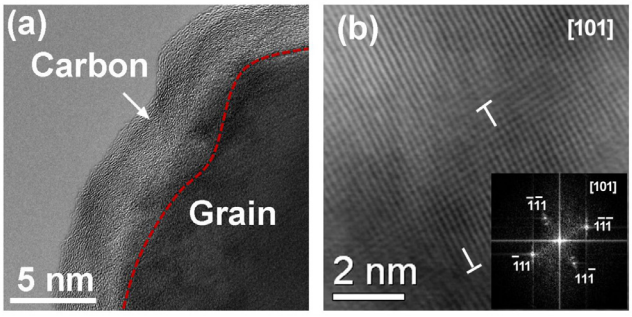

Fig. 11. (a) TEM image of fragmented n-SiC shows highly strained at interface carbon. (b) Bright field STEM image showing edge dislocations inside a nano SiC grain.

3.7. Density functional theory molecular dynamics simulations

In order to understand the essential role of interface graphite phases at grain boundaries, we have carried out DFT-MD simulations of finite shear deformation on the model combining SiC and graphite. Fig. 12a displays the shear stress–strain relations for the shear deformation for the 10% compression case with 19.07 GPa stress in z axis. The shear stress increases from the initial zero to the end structure, reaching the maximum value of $\tau = 22.58$ GPa at 0.67 shear strain. During the whole shear process, no significant local deformation is observed (Fig. 12b and c). Thus, the overall system experiences an elastic deformation with a non-monotonically increase in stress–strain relationship before 0.2 shear strain. For example, from 0.06 to 0.08 strain and from 0.14 to 0.19 strain, although the shear strain increases, the shear stress drops slightly. The reasons are two folds: for one thing, the graphite layers can easily slide under shearing; for the other thing, when experiencing a large stress concentration, the loads on SiC transfer to laminar graphite, relaxing the system stress, preventing the SiC structure from plastic deformation or further crack initiating. Thus, our simulations results confirm our experimental conclusion that interface carbon does play an impor-

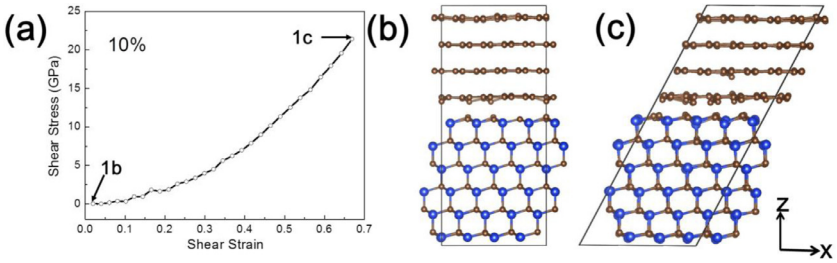

Fig. 12. Pure shear deformation for the combined model of SiC and graphite with pre-compressed rate of 10% in *z* axis. The shear model is made of $(111)\langle\bar{2}11\rangle$ slip system for SiC and $(001)\langle100\rangle$ slip system for graphite. (a) simulated stress–strain curves for 10% pre-compressed systems. (b-c) 10% compression structure at 0.02 and 0.67 shear strain showing no apparent structural change during the whole shear process.

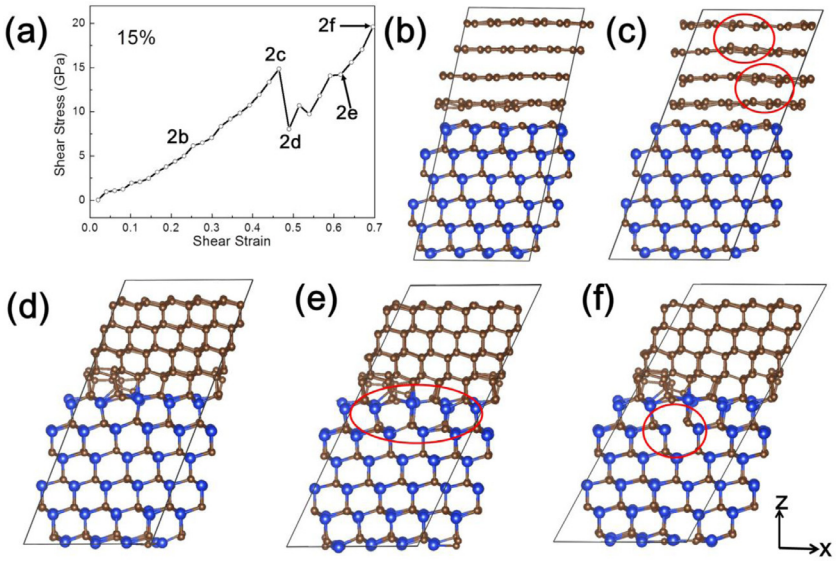

Fig. 13. Pure shear deformation for the combined model of SiC and graphite with pre-compressed rate of 15% in *z* axis. The shear model is made of $(111)\langle\bar{2}11\rangle$ slip system for SiC and $(001)\langle100\rangle$ slip system for graphite. (a) simulated stress–strain curves for 15% pre-compressed systems. (b-f) Snapshots of 15% pre-compressed structures evolution under pure shear deformation showing the successive processes of interactions between interface carbon and SiC grain at grain boundaries: (b-c) structures showing slight shift of carbon atoms in graphite towards carbon atoms in adjacent layers; (d-e) structures after transformation to diamond phase with complex bond formation between SiC and diamond interface and with dislocations in SiC; (f) structure at 0.696 shear strain corresponding to bond breakings between Si and C atoms in SiC.

tant role in relaxation of stress concentration at grain boundaries in SiC nanograins.

Fig. 13a displays the shear stress-shear strain relations for the shear deformation in the 15% compression case with 37.05 GPa stress in *z* axis. First, the shear stress increases as the shear strain increases to 0.46 shear strain, reaching 14.87 GPa with a varied increase rate due to graphite sliding and loads transfer as discussed above. In addition, during these periods, along with laminar graphite sliding, carbon atoms from different stacking graphite layers and from interfacial SiC are slightly shifted along the *z* direction forming out-of-plane deformation, which indicates the strong Van der Waals interactions between adjacent carbon atoms (Fig. 13b and c). Phase transformation starts at the shear strain of 0.49, leading to a sharp drop in shear stress due to the shifted carbon atoms are bonded to the carbon atoms from neighbor layers not only to those in adjacent graphite layers, but also to those in the SiC layers, as shown in Fig. 13d, leading to the graphite forming the diamond phase. The transition shear stress is 14.87 GPa at uniaxial stress of 44.02 GPa, which is lower than the transformation pressure in previous DFT simulations [49], indicating that SiC might be helpful to the strain-induced transformations for graphite to diamond transition. This is because the interactions between carbon atoms from graphite and SiC make them form bonds at interface in an easy way. With the gradual increase of shear strain to 0.62 (Fig. 13e), the shear stress increases and relaxes. Dislocations of Si atoms were observed in SiC. A further shear straining leads to bond breakage between Si and C atoms at 0.70 strain (Fig. 13f).

4. Discussion

The brittle failure of ceramics is often governed by crack nucleation and propagation caused by various reasons such as rigid atomic structure, inclusions, porosity and secondary phases [4–6,45,50–52]. Therefore, damage mechanisms depend on the nature of microstructure, which need to be effectively tuned against cracks and failure. In this study, we found that nanocrystalline SiC containing homogenous nano-layered graphitic carbon at the grain boundaries is effective against the crack initiation and failure.

The measured K_{IC} values of n-SiC ranges from 3.3 to 5.4 MPa $m^{1/2}$ (Fig. 5), which are significantly higher as compared to microcrystalline SiC values in the range of 2.3 and 3.5 MPa $m^{1/2}$ [1,10,12,23]. Also, it is slightly higher than the reported nanocrystalline SiC films ranging from 3 to 5 MPa $m^{1/2}$ for the grain size of 5 to 20 nm [25]. The enhanced K_{IC} of n-SiC compared to microcrystalline SiC and nanocrystalline films can be attributed to the uniformly distributed nano-layered graphite at the grain boundaries. The crack propagation near the indentation corner of n-SiC (Supplementary Fig. S3) proceeds in the mode of intergranular fracture, which is different from microcrystalline SiC where crack propagation is accompanied by transgranular fracture mode [4,5,11,12]. Further, the strength of n-SiC was found as high as ~11 GPa, which is almost 3–4 times higher than that of bulk microcrystalline SiC (2–4 GPa) [47,48].

SEM images acquired from the deformed n-SiC micropillar revealed the intergranular fracture, which is different from characteristic brittle cleavage in microcrystalline SiC (Fig. 10d). It is evident from the engineering stress–strain curves that the n-SiC can sustain large strain around 3% as well as detectable plasticity at high pressures above 8 GPa (Fig. 10). Previously, plasticity was observed in a single crystal SiC micropillar with a diameter size below 0.65 μm under a high applied stress of 7.8 GPa [53–55]. Recently, Wang et al. reported the localized plasticity by laser shock processing, when the strength of SiC increased from ~4 to 7 GPa [56]. Thus, these experimental observations are consistent with our findings that plastic deformation at room temperature could occur in polycrystalline SiC at high strength above 7 GPa by preventing crack initiation.

Meanwhile, experimentally measured yield strength (σ_y) and fracture toughness (K_{IC}) (Figs. 5 and 9) were substituted in Griffith's equation to estimate critical crack length of n-SiC [57].

$$a = \frac{K_{IC}^2}{2\pi\sigma_Y^2} \quad (4)$$

The obtained critical crack length (a) values of n-SiC are between 0.02 μm and 0.08 μm, which is 2–3 orders of magnitude lower than the typical mode-I displacement crack size (a_t-1 μm) in brittle ceramics [52,58,59]. Our TEM examinations (Fig. 8) within deformation region of n-SiC show the elimination of fine pores of about ~3% with the assistance of soft interface graphitic phase. No cracks can be found within the indentation region indicating the intrinsic toughening [5,6]. The HRTEM image in Fig. 9 reveals the disordered carbon at grain boundaries and triple junction of deformed n-SiC. This indicates that the localized plastic deformation by GB sliding can be accommodated to prevent crack initiation. Also, Raman spectra acquired from the indentation region of n-SiC showed decrease of carbon intensity peaks as compared to pristine surface. This can be understood on the basis of the carbon-carbon bond compression in the soft graphitic phase, which lowers the crystallinity during high contact pressures (Fig. 6). In addition, shear sliding of fine grains upon deformation leads to the emission of dislocations along {111}<110> slip system, which provides the direct evidence of plasticity in brittle SiC ceramic.

Recent theoretical studies and computational simulations predicted that the Peierls stress is about 5–12 GPa and Schmidt factor is about ~0.4 for a 3C-SiC {111}<110> slip system [59–61]. The critical resolved shear stress (τ) for n-SiC achieved by multiplying the maximum uniaxial strength (σ) with the Schimdt factor ($\cos\varphi \cos\lambda$) falls in the range of ~3 to 5 GPa. Although τ value of n-SiC is slightly lower than the estimated value for single crystal {111}<110> slip systems, the suppression of the nanocrack nucleation near triple junctions due to the presence of weak carbon phase may give rise to the enhanced plasticity by the combined action of lattice dislocation slip and grain boundary sliding as dominant deformation modes [28,62]. Szlufarska et al. applied MD simulations to examine the indentation of n-SiC and revealed that the coexisting brittle grains and amorphous grain boundary phases result in a GB sliding leading to superhigh hardness around 39 GPa [28]. Our current experimental study on n-SiC showed GB sliding can significantly promote plastic deformation and enhance the strength.

The phase transformation from graphitic carbon to amorphous carbon at grain boundaries in our experiment might arise from pre-existing defects such as vacancies, voids or cavities (see Fig. 2b and c). However, our DFT-MD simulations are based on the perfect structure so that graphite phase can be easily achieved (Figs. 12 and 13). Therefore, our simulations are consistent with the experimental measurements and provide atomic insights to uncover that dislocations could be induced through GBs sliding and the phase transformation plays an important role in stress relaxation in stress concentrated grain boundaries.

5. Conclusions

In summary, GB sliding appears to be the underlying mechanism for plastic deformation as well as the overall enhanced mechanical properties of n-SiC. The significantly enhanced fracture toughness and uniaxial compressive strength as compared to microcrystalline SiC is mainly attributed to nano-size effect and soft interface phase at the grain boundaries. The engineering stress–strain relationship of n-SiC demonstrates that the micropillars can sustain very large strain of ~3% with the assistance of weak carbon interface contributing to the detectable plasticity at room temperature. The cross-sectional TEM of deformed n-SiC showed transition to amorphous carbon grain boundaries, grain sliding and dislocation formation. Further, DFT-MD simulations provide insights from atomistic perspective to confirm our experiments' conclusion that interface carbon does play an important role, such as by sliding and phase transformation, in relaxation of stress concentration at grain boundaries, and further causes dislocations.

Declaration of interest

The authors declare no competing interests.

Acknowledgments

This research work was supported by National Natural Science Foundation of China (Grant No. 51850410501) and MOST 973 of China (Grant No. 2015CB856800). Q. A. and D. G are supported by National Science Foundation (CMMI-1727428).

Supplementary materials

Supplementary material associated with this article can be found, in the online version, at doi:10.1016/j.mtla.2019.100394.

References

[1] G.L. Harris (Ed.). Properties of Silicon Carbide. No. 13. Let (1995).
[2] S.M. Spearing, Materials issues in microelectromechanical systems (MEMS), Acta Mater. 48 (2000) 179–196.
[3] A.G. Evans, Perspective on the development of high-toughness ceramics, J. Am. Ceram. Soc. 73 (1990) 187–206.
[4] H. Wang, K.T. Ramesh, Dynamic strength and fragmentation of hot-pressed silicon carbide under uniaxial compression, Acta Mater. 52 (2004) 335–367.
[5] R.O. Ritchie, The conflicts between strength and toughness, Nat. Mater. 10 (2011) 817–822.
[6] W.E. Lee, M. Rainforth, Ceramic Microstructures: Property Control by Processing, Springer Science & Business Media, 1994.
[7] J.M. Fernández, A. Munoz, A.R. de Arellano López, F.M. Valera Feria, A. Dominguez-Rodriguez, M. Singh, Microstructure-mechanical properties correlation in siliconized silicon carbide ceramics, Acta Mater. 5 (2003) 3259–3275.
[8] P.D. Miller, J.G. Lee, I.B. Culter, The reduction of silica with carbon and silicon carbide, J. Am. Ceram. Soc. 62 (1979) 147–149.
[9] D.H. Stutz, S. Prochazka, J. Lorenz, Sintering and microstructure formation of β-silicon carbide, J. Am. Ceram. Soc. 68 (1985) 479–482.
[10] R.H. Hannink, Y. Bando, H. Tanaka, Y. Inomata, Microstructural investigation and indentation response of pressureless-sintered α- and β-SiC, J. Mater. Sci. 23 (1988) 2093–2101.
[11] W.N. Sharpe, O. Jadaan, G.M. Beheim, G.D. Quinn, N.N. Nemeth, Fracture strength of silicon carbide microspecimens, J. Microelectromech. Syst. 14 (2005) 903–913.
[12] G. Orange, H. Tanaka, G. Fantozzi, Fracture toughness of pressureless sintered silicon carbide. A comparsion of K_{IC} measurement methods, Ceram. Int. 13 (1987) 159–165.
[13] K. Negita, Effective sintering aids for silicon carbide ceramics: reactivities of silicon carbide with various additives, J. Am. Ceram. Soc. 69 (1986) C–308-310.
[14] J. Zhao, L.C. Stearns, M.P. Harmer, H.M. Chan, G.A. Miller, R.F. Cook, Mechanical behavior of alumina-silicon carbide, nanocomposites, J. Am. Ceram. Soc. 76 (1993) 503–510.
[15] A.F. Zimmerman, G. Palumbo, K.T. Aust, U. Erb, Mechanical properties of nickel silicon carbide nanocomposites, Mater. Sci. Eng. A 328 (2002) 137–146.
[16] J.J. Cao, W.J. MoberlayChan, L.C. De Jonghe, C.J. Gilbert, R.O. Ritchie, In situ toughened silicon carbide with Al-B-C additions, J. Am. Ceram. Soc. 79 (1996) 461–469.
[17] N.P. Padture, In situ-toughened silicon carbide, J. Am. Ceram. Soc. 77 (1994) 519–523.
[18] M. Nader, F. Aldinger, M.J. Hoffmann, Influence of the α/β-SiC phase transformation on microstructural development and mechanical properties of liquid phase sintered silicon carbide, J. Mater. Sci. 34 (1999) 1197–1204.
[19] M. Keppeler, H.G. Reichert, J.M. Broadley, G. Thurn, I. Wiedmann, F. Aldinger, High temperature mechanical behaviour of liquid phase sintered silicon carbide, J. Euro. Ceram. Soc. 18 (1998) 521–526.
[20] H. Gleiter, Nanostructured materials: basic concepts and microstructure, Acta Mater. 48 (2000) 1–29.
[21] M. Mitomo, Y.K. Kim, H. Hirotsuru, Fabrication of silicon carbide nanoceramics, J. Mater. Res. 11 (1996) 1601–1604.
[22] J. Gubicza, S. Nauyoks, L. Balogh, J. Labar, T.W. Zerda, T. Ungár, Influence of sintering temperature and pressure on crystallite size and lattice defect structure in nanocrystalline SiC, J. Mater. Res. 22 (2007) 1314–1321.
[23] R. Vassen, D. Stöver, Processing and properties of nanograin silicon carbide, J. Am. Ceram. Soc. 82 (1999) 2585–2593.
[24] Y. Shinoda, T. Nagano, H. Gu, F. Wakai, Superplasticity of silicon carbide, J. Am. Ceram. Soc. 82 (1999) 2916–2918.
[25] F. Liao, S.L. Girshick, W.M. Mook, W.W. Gerberich, M.R. Zachariah, Superhard nanocrystalline silicon carbide films, Appl. Phys. Lett. 86 (2005) 171913.
[26] M.A. Meyers, A. Mishra, D.J. Benson, Mechanical properties of nanocrystalline materials, Prog. Mater. Sci. 51 (2006) 427–556.

[27] D. Wolf, V. Yamakov, S.R. Phillpot, A. Mukherjee, H. Gleiter, Deformation of nanocrystalline materials by molecular-dynamics simulation:relationship to expertiments? Acta Mater 53 (2005) 1–40.
[28] I. Szlufarska, A. Nakano, P. Vashishta, A crossover in the mechanical response of nanocrystalline ceramics, Science 309 (2005) 911–914.
[29] G. Kresse, J. Hafner, Ab initio molecular dynamics for liquid metals, Phys. Rev. B 47 (1993) 558–561.
[30] G. Kresse, J. Furthmüller, Efficency of ab-initio total energy calculations for metals and semiconductors using a plane-wave basis set, Comput. Mater. Sci. 6 (1996) 15–50.
[31] J. Paier, R. Hirschl, M. Marsman, G. Kresse, The Perdew–Burke–Ernzerhof exchange–correlation functional applied to the G2-1 test set using a plane-wave basis set, J. Chem. Phys. 122 (2005) 234102.
[32] G. Kresse, D. Joubert, From ultrasoft pseudopotentials to the projector augmented-wave method, Phys. Rev. B 59 (1999) 1758–1775.
[33] P.E. Blöchl, O. Jepsen, O.K. Andersen, Improved tetrahedron method for Brillouin–zone integrations, Phys. Rev. B. 49 (1994) 16223–16233.
[34] S. Grimme, S. Ehrlich, L.J. Goerigk, Effect of the damping function in dispersion corrected density functional theory, J. Comput. Chem. 32 (2011) 1456–1465.
[35] V.V. Pujar, J.D. Cawley, Effect of stacking faults on the X-ray diffraction profiles of β-SiC powders, J Am. Ceram. Soc. 78 (1995) 774–782.
[36] C.A. Schuh, Nanoindentation studies of materials, Mater. Today 9 (2006) 32–40.
[37] G.M. Pharr, W.C. Oliver, F.R. Brotzen, On the generality relationship among contact stiffness, contact area, and elastic modulus during indentation, J. Mater. Res. 7 (1992) 613–617.
[38] M.T. Laugier, Palmqvist indentation toughness in WC-Co composites, J. Mater. Sci. Lett. 6 (1987) 897–900.
[39] W.D. Nix, H. Guo, Indentation size effects in crystalline materials: a law for strain gradient plasticity, J. Mech. Phys. Solids 46 (1998) 411–425.
[40] F. Ouchterlony, Stress intensity factors for the expansion loaded star crack, Eng. Fract. Mech. 8 (1976) 447–448.
[41] S. Rohmfeld, M. Hundhausen, L. Ley, Raman scattering in ploycrystalline 3C-SiC: influence of stack faults, Phys. Rev. B 58 (1998) 9858–9862.
[42] Y. Wang, D.C. Alsmeyer, R.L. McCreery, Raman spectroscopy of carbon materials: structural basis of observed spectra, Chem. Mater. 2 (1990) 557–563.
[43] M.A. Pimenta, G. Dresselhaus, M.S. Dresselhaus, L.G. Cancado, A. Jorio, R. Saito, Studying disorder in graphite-based systems by Raman spectroscopy, Phys. Chem. Chem. Phys. 9 (2007) 1276–1291.
[44] L.A. Giannuzzi, F.A. Stevie, Introduction to Focused Ion Beams: Instrumentation, Theory, Techniques and Practice, Springer Science & Business Media, 2004.
[45] K.M. Reddy, P. Liu, A. Hirata, T. Fujita, M.W. Chen, Atomic structure of amorphous shear bands in boron carbide, Nat. Commun. 4 (2013) 2483.
[46] K.M. Reddy, J.J. Guo, Y. Shinoda, T. Fujita, A. Hirata, J.P. Singh, J.W. McCauley, M.W. Chen, Enhanced mechanical properties of nanocrystalline boron carbide by nanoporosity and interface phases, Nat. Commun. 3 (2012) 1052.
[47] S. Sarva, S. Nemat-Nasser, Dynamic compressive strength of silicon carbide under uniaxial compression, Mater. Sci. Eng. A 317 (2001) 140–144.
[48] J.F. Shackelford, Y.H. Han, S. Kim, S.H. Kwon, CRC Materials Science and Engineering Handbook, CRC Press, 2016.
[49] G. Yang, Y. Ma, Q. An, V. Levitas, Y. Zhang, B. Feng, J. Chaudhuri, W.A. Goddard III, Shear driven formation of nano-diamonds at sub-gigapascals and 300 K, Carbon 146 (2019) 364–368.
[50] E.D. Case, J.R. Smyth, O. Hunter Jr., Microcracking in large-grain Al_2O_3, Mater. Sci. Eng. 51 (1981) 175–179.
[51] K.M. Reddy, A. Hirata, P. Liu, T. Fujita, T. Goto, M.W. Chen, Shear amorphization of boron suboxide, Scr. Mater. 76 (2014) 9–12.
[52] M. Bengisu, Engineering Ceramics, Springer Science & Business Media, 2013.
[53] C. Shuh, H.H. Jin, W.J. Kim, J.Y. Park, Mechanical properties and deformation of cubic silicon carbide micropillars in compression at room temperature, J. Am. Ceram. Soc. 95 (2012) 2944–2950.
[54] X.D. Han, Y.F. Zhang, K. Zhang, X.N. Zhang, Z. Zhang, Y.J. Hao, X.Y. Guo, J. Yuan, Z.L. Wang, Low temperature in situ large strain plasticity of ceramic SiC nanowires and its atomic-scale mechanism, Nano Lett. 7 (2007) 452–457.
[55] S. Kiani, K. Leung, V. Radmilovic, A. Minor, J.M. Yang, D. Warner, S. Kodambaka, Dislocation glide controlled room-temperature plasticity in 6H-SiC single crystals, Acta Mater. 80 (2014) 400–406.
[56] F. Wang, X. Yan, C. Zhang, L. Deng, Y. Lu, M. Nastasi, B. Cui, Localized plasticity in silicon carbide ceramics induced by laser shock processing, Materialia 6 (2019) 100265.
[57] A.A. Griffith VI, The phenomena of rupture and flow in solids, Philos. Trans. R. Soc. A 221 (1921) 163–198.
[58] C.E. Renshaw, E.M. Schulson, Universial behaviour in compressive failure of brittle materials, Nature 412 (2001) 897 890.
[59] M. Tang, S. Yip, Lattice instability in β-SiC and simulation of brittle fracture, J. Appl. Phys. 76 (1994) 2719–2725.
[60] H.P. Chen, R.K. Kalia, A. Nakano, P. Vashishta, I. Szlufarska, Multimillion-atom nanoindentation simulation of crystalline silicon carbide orientation dependence and anisotropic pile up, J. Appl. Phys. 102 (2007) 063514.
[61] H.L. Zhang, The properties of shockley partials in crytsalline cubic silicon carbide (3C-SiC): core width and Peierls stress, Phys. Rev. B 406 (2011) 1323–1325.
[62] D. Guo, S. Song, R. Luo, W.A. Goodard III, M.W. Chen, K.M. Reddy, Q. An, Grain boundary silding and amorphization is responsible for the reverse Hall–Petch relation in superhard nanocrystalline boron carbide, Phys. Rev. Lett. 121 (2018) 145504.